Contact between shear-deformable beams with elliptical cross-sections

M. Magliulo, A. Zilian, L.A.A. Beex*

Institute of Computational Engineering, Faculty of Science, Technology and Communication, University of Luxembourg, Maison du Nombre, 6, Avenue de la Fonte, 4364 Esch-sur-Alzette, Luxembourg

Abstract

Slender constituents are present in many structures and materials. In associated mechanical models, each slender constituent is often described with a beam. Contact between beams is essential to incorporate in mechanical models, but associated contact frameworks are only demonstrated to work for beams with circular cross-sections. Only two studies have shown the ability to treat contact between beams with elliptical cross-sections, but those frameworks are limited to point-wise contact, which narrows their applicability. This contribution presents initial results of a framework for shear-deformable beams with elliptical cross-sections if contact occurs along a line or at an area (instead of at a point). This is achieved by integrating a penalty potential over one of the beams' surfaces. Simo-Reissner Geometrically Exact Beam (GEB) elements are employed to discretise each beam. As the surface of an assembly of such beam elements is discontinuous, a smoothed surface is introduced to formulate the contact kinematics. This enables the treatment of contact for large sliding displacements and substantial deformations.

Keywords: beams, contact, shear-deformable, elliptical cross-sections, wire ropes, ropes

1. Introduction

Paper materials (wood fibres [1, 2, 3, 4, 5]), fabrics (yarns [6, 7, 8, 9, 10]), and metal foams (struts [11, 12, 13, 14, 15]) are examples of materials with slender components in their microstructure. Micromechanical models of such materials often represent each slender constituent as a beam, which yields a string of beam finite elements when discretized [16] (or springs [17, 18]). In most cases, contact between the slender constituents is essential to be incorporated. Almost all contact frameworks have however focused on beams with circular cross-sections. To the best of the authors' knowledge, only two frameworks are demonstrated to work for beams with non-circular cross-sections ([19] and [20]), but they are limited by the fact that contact can only occur in a point-wise manner.

In many applications however, the slender constituents do not come with circular cross-sections and contact does not occur at a single point. This contribution therefore aims to partially fill this gap by proposing an algorithm that treats contact between shear-deformable beams with elliptical cross-sections. The scheme is tailored for contact to occur at an area on the beams' surfaces, instead of only at a pair of surface points. Consequently, it is more widely applicable and can for instance

*corresponding author: L.A.A. Beex, Lars.Beex@uni.lu

be applied to the cases of Fig. 1, which cannot be treated by point-wise contact schemes.
The proposed contact scheme seeds many quadrature points on the surface of beams and determines which points penetrate the surrounding beams. A measure of penetration is established for each penetrating surface point, which is used in a penalty potential that is incorporated in the potential energy of the system in order to repel penetrating beams.
The scheme is applied to beam elements with two nodes based on the geometrically exact beam (GEB) theory. As the surfaces of strings of such beam elements are only C^0-continuous, and may even be C^{-1}-continuous, the contact scheme works on a smooth (approximated) surface. The smooth surface is obtained by smoothing the strings' centroid lines using Bézier curves. The kinematic variables (i.e. the displacements and rotations) are also re-interpolated. The capabilities of the contact scheme are demonstrated for several numerical test cases. These include the twisting of wire ropes. We show that cross-sectional shapes may have a critical influence on the deformations. The introduced contact framework remains to converge even when the structures in contact undergo large sliding displacements and/or large rotations and/or large deformations. We also demonstrate that large sliding displacements of the contacting surfaces can occur without the chattering phenomenon [21] thanks to the artificially smoothed surface.

In the next section, we briefly discuss the kinematics of the GEB theory. Section 3 discusses the contact framework, still in the space-continuous setting. In Section 4, we discretise beams with beam elements with two nodes. We amongst others discuss why the surface of connected beam elements is C^0-continuous at best for this type of beam. The smooth approximations of the discretized beams' surfaces is discussed next and the proposed contact framework is adapted to them. Section 5 presents initial results. The contribution closes with some conclusions and an outlook.

(a) Two parallel beams.

(b) Two beams folded around each other.

Figure 1: Some examples in which the shortest distance between two surfaces is not uniquely or poorly defined, thus preventing the application of a point-wise contact force.

2. Kinematics

The Simo-Reissner Geometrically Exact Beam (GEB) theory ([22, 23, 24, 25, 26, 27, 28]) of shear-deformable beams with rigid cross-sections is used in this contribution. A beam is characterized by centroid line $\mathbf{x}_c(h_1) : [0, L_0] \to \mathbb{R}^3$ (constituted from the center of gravity of its sections) and by the orientations of the sections (see Fig. 2). h_1 is the arc-length parameter of the centroid line of the beam in the reference configuration and L_0 its reference length.Rigid cross-sections are not necessarily orthogonal to $\mathbf{x}_c$ in the current (deformed) configuration if shear deformation is present.

A field of rotation tensor $\mathbf{\Lambda}(h_1) : [0, L_0] \rightarrow SO(3)$ is used to orientate the sections in the current configuration.

Material points on the beam's centroid line

The centroid line in the current configuration, $\mathbf{x}_c(h_1)$, is related to the centroid line in the reference configuration, $\mathbf{X}_c(h_1)$, by:

$$\mathbf{x}_c(h_1) = \mathbf{X}_c(h_1) + \mathbf{u}_c(h_1), \tag{1}$$

where $\mathbf{u}_c(h_1) : [0, L_0] \rightarrow \mathbb{R}^3$ denotes the displacement field of the centroid line.

Material points in the rest of the beam

To locate material points on the beam's centroid line (in the reference and deformed configurations), only h_1 is needed. To locate the remaining material points however, we need to consider cross-sections, which are parametrised by h_2 and h_3.

The location vector pointing towards a material point with local coordinates $\mathbf{h} = [h_1, h_2, h_3]$ that is not located on the centroid line can be expressed in the reference configuration as follows:

$$\mathbf{X}(\mathbf{h}) = \mathbf{X}_c(h_1) + \mathbf{V}(\mathbf{h}), \tag{2}$$

and in the deformed configuration as:

$$\mathbf{x}(\mathbf{h}) = \mathbf{x}_c(h_1) + \mathbf{v}(\mathbf{h}), \tag{3}$$

where $\mathbf{V}$ and $\mathbf{v}$ point from the centroid line to the material point and both lie in the cross-sectional plane associated with h_1. $\mathbf{V}$ works in the reference configuration and $\mathbf{v}$ in the deformed configuration. These two vectors can be written as follows:

$$\mathbf{V}(\mathbf{h}) = h_2\mathbf{e}_{02}(h_1) + h_3\mathbf{e}_{03}(h_1), \tag{4}$$

$$\mathbf{v}(\mathbf{h}) = \mathbf{\Lambda}(h_1)(h_2\mathbf{e}_{02}(h_1) + h_3\mathbf{e}_{03}(h_1)), \tag{5}$$

where $\mathbf{e}_{02}(h_1)$ and $\mathbf{e}_{03}(h_1)$ form an orthonormal basis with $\mathbf{e}_{01}(h_1)$ (see Fig. 2). In Eq. (5), $\mathbf{\Lambda} \in SO(3)$ denotes the rotation tensor rotating the section attached to $\mathbf{X}_c$ in the reference configuration.

In the reference configuration the (unit) normal vector to the section attached to $\mathbf{X}_c$, $\mathbf{e}_{01}$, verifies:

$$\mathbf{e}_{01} = \frac{\partial \mathbf{X}_c}{\partial h_1}, \tag{6}$$

because no shear deformation is present. As mentioned above however, the normal to the section in the current configuration is not necessarily aligned with the tangent direction to the centroid line, which means that:

$$\mathbf{\Lambda}\mathbf{e}_{01} \neq \frac{\partial \mathbf{x}_c}{\partial h_1}. \tag{7}$$

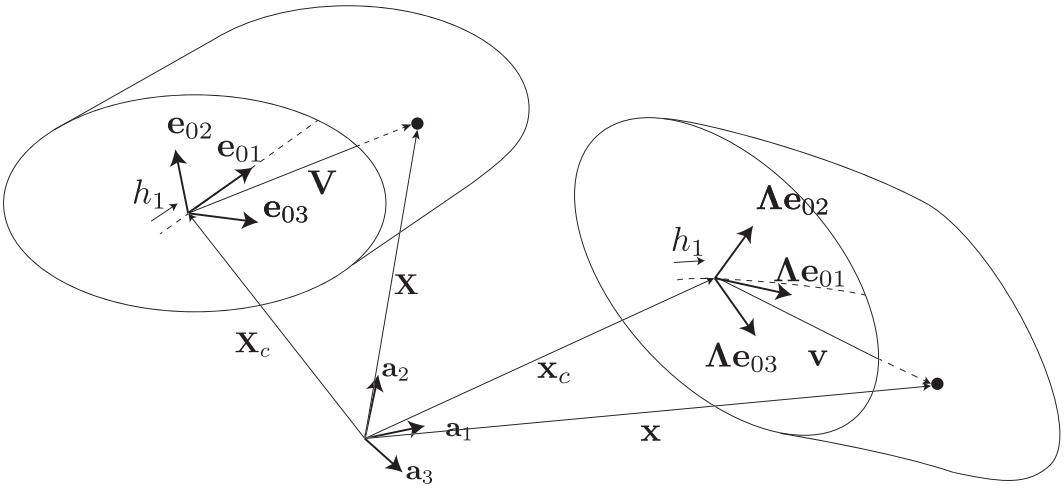

Figure 2: A surface point $\mathbf{X}$ in the reference configuration (black circle) obtained by adding location vector $\mathbf{X}_c$ and a vector $\mathbf{V}$ in the plane $(\mathbf{e}_{02}, \mathbf{e}_{03})$ of the section attached to $\mathbf{X}_c$. The same material point is represented in the deformed configuration. The global basis $\{\mathbf{a}_1, \mathbf{a}_2, \mathbf{a}_3\}$ as well as the local basis $\{\mathbf{e}_{01}, \mathbf{e}_{02}, \mathbf{e}_{03}\}$ attached to the $\mathbf{X}_c$ in the reference configuration and the local basis $\{\mathbf{e}_1, \mathbf{e}_2, \mathbf{e}_3\}$ attached to the same point in the deformed configuration are also presented. These three basis are orthonormal.

3. Contact framework

The contact framework is based on the integration of a surface-specific contact potential over the surface of one of the beams. To this end, contact points are seeded on the surface of one of the two beams in contact. We check for each of these surface points if it penetrates the other beam. If a surface point is indeed penetrated, a contribution to a contact potential is added. The suggested scheme is thus a type of master-slave approach [29] which asymmetrically treats contact, in contrast to [19, 20, 30, 31].
The surface of both beams is explicitly taken into account. This is different from the approaches in [32, 33, 34] in which the centroid lines are used to formulate contact due to the limitation of circular sections. A penalty approach is adopted here to regularize unilateral contact conditions. It allows some interpenetration between the bodies, which can be interpreted as the deformation of the rigid cross-sections in case of contact.

3.1. Projection

In this subsection, we discuss for a single surface point how we determine if it penetrates another beam. We start with the definition of a fixed surface point. We denote its local coordinates by $\mathbf{h}^{s1}$ which remain constant. Superscript 1 means that we refer to the 1^{st} beam as the slave body and superscript s means that the point refers to a material point on the surface (and not to a material point inside the beam). In a deformed configuration, the location of this point is expressed in the global coordinate system by $\mathbf{x}^{s1} = \mathbf{x}^1(\mathbf{h}^{s1})$. Similarly as for the slave body (beam 1), we denote the location of a material point on the surface of the master body by $\mathbf{h}^{s2}$ in terms of the local coordinates of the beam and by $\mathbf{x}^{s2} = \mathbf{x}^2(\mathbf{h}^{s2})$ in terms of the global coordinates.

It is important to note however that if elliptical sections are used, only two independent variables are required to locate a material point on a beam's surface ([19]). We therefore write $\mathbf{h}^{s1} = \mathbf{h}^{s1}(\underline{h}^1)$ and $\mathbf{h}^{s2} = \mathbf{h}^{s2}(\underline{h}^2)$ where $\underline{h}$ denotes the column with these two independent variables. One of them is $h_1 \in [0, L]$, while the second one is $\beta \in [0, 2\pi]$ such that h_2 and h_3 in Eqs. (4) and (5) are given by:

$$h_2 = a\ cos(\beta) \tag{8}$$

and

$$h_3 = b\ sin(\beta) \tag{9}$$

respectively, where a and b denote the dimensions of the elliptical section in the two principal directions.

We define the projection based on Fig. 3 and state that vector $\mathbf{x}^{s1} - \mathbf{x}^{s2}$, must point in the same direction as the vector $\mathbf{x}^{s2} - \mathbf{x}_c^2$. This is verified when the following residual is zero:

$$\mathbf{f}(\mathbf{h}^{s2}(\underline{h}^2), g_N) = \mathbf{x}^{s1} - g_N \frac{\mathbf{x}^{s2} - \mathbf{x}_c^2}{\|\mathbf{x}^{s2} - \mathbf{x}_c^2\|} - \mathbf{x}^{s2}, \tag{10}$$

where g_N is an independent variable, which is negative in case of penetration and non-negative otherwise. Thus g_N will be used as a measure of penetration in the following. In Eq. (10) we used the vector $\frac{\mathbf{x}^{s2} - \mathbf{x}_c^2}{\|\mathbf{x}^{s2} - \mathbf{x}_c^2\|}$ as an approximation of the normal to the master body $\mathbf{n}^2$ at surface point $\mathbf{x}^{s2}$. This choice is justified by the fact that $\mathbf{n}^2$ changes abruptly in the regions of high curvatures of the surface. This can cause convergence problems at the global level because of the direction of the contact forces may change significantly from one (global) iteration to the next. We thus want to find column $\bar{\underline{q}} = [\bar{\underline{h}}^2, \bar{g_N}]^T$ for which $\mathbf{f}(\bar{\underline{q}}) = \mathbf{0}$. Here and in the following, a bar over a quantity indicates that this quantity is evaluated at the solution of Eq. (10).

We solve $\mathbf{f}(\bar{\underline{q}}) = \mathbf{0}$ this by linearising $\mathbf{f}$ in Eq. (10) and applying Newton's method, which we write as follows:

$$\mathbf{f}(\underline{q}^e) + \underline{\mathbf{H}}(\underline{q}^e)\, \Delta\underline{q} = \mathbf{0}, \tag{11}$$

where $\underline{q}^e$ denotes the previous estimate of $\bar{\underline{q}}$ and $\Delta\underline{q}$ denotes its update. Row of vectors $\underline{\mathbf{H}}$ is given by:

$$\underline{\mathbf{H}}(\underline{q}^e) = \left.\frac{\partial \mathbf{f}}{\partial(\underline{q})}\right|_{\underline{q}^e}. \tag{12}$$

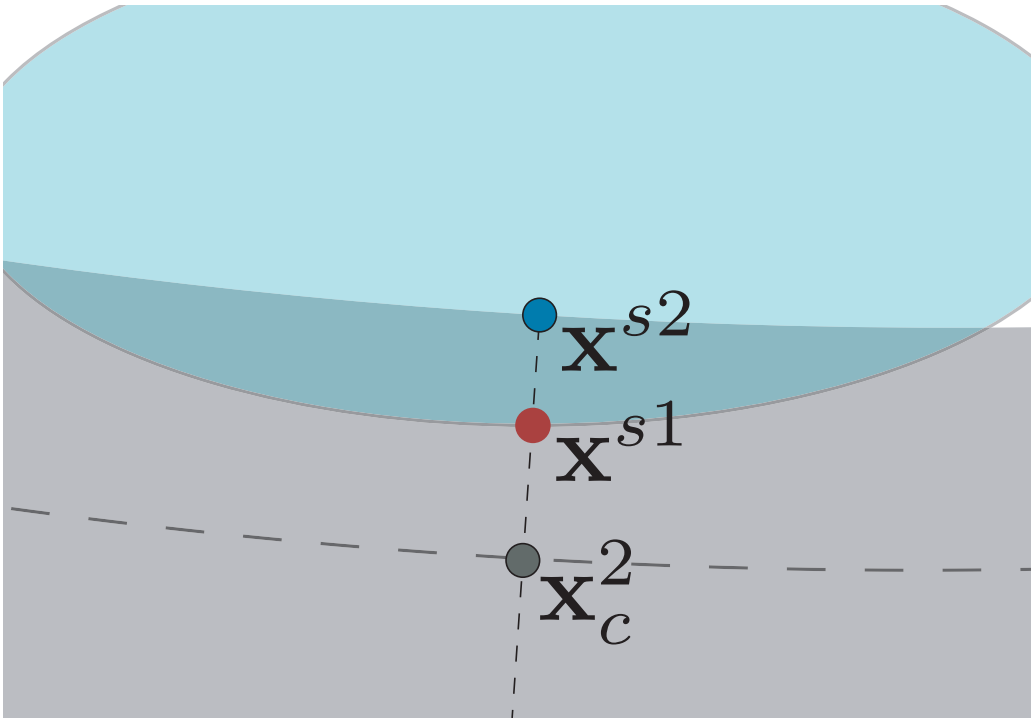

Figure 3: Penetrated slave surface point $\mathbf{x}^{s1}$ (in red). The slave section on which $\mathbf{x}^{s1}$ lies is presented in translucent blue. The centroid line of the master beam (grey) is presented by a thick dashed line. The master surface point at the solution of the projection problem is presented in blue. In this particular configuration, the vectors $\mathbf{x}^{s2} - \mathbf{x}_c^2$ and $\mathbf{x}^{s2} - \mathbf{x}^{s1}$ are colinear and Eq. (10) is verfied if $g_N = -\left\|\mathbf{x}^{s1} - \mathbf{x}^{s2}\right\|$.

3.2. Contact potential

As mentioned before, we use a penalty potential to limit penetration of surface point $\mathbf{x}^{s1}$ in body B^2. We use the following penalty potential to do so:

$$\Pi_{pen}(\underline{p}^1, \underline{p}^2, \underline{\bar{q}}(\underline{p}^1, \underline{p}^2)) = \begin{cases} \frac{\epsilon}{2}\left(\bar{g}_N^2 - T\bar{g}_N + \frac{T^2}{3}\right) & \text{if} \quad \bar{g}_N < T \\ \frac{\epsilon}{6T}\bar{g}_N^3 & \text{if} \quad T \leqslant \bar{g}_N < 0 \\ 0 & \text{if} \quad \bar{g}_N \geqslant 0 \end{cases}, \tag{13}$$

where ϵ denotes the user-selected penalty stiffness and $\underline{p}^i$ denotes the fields of kinematic variables of the i^{th} beam that are involved in the contact. In Eq. (13), T denotes a numerical parameter used to switch between a cubic and a quadratic penalty potential. The cubic potential is effective to regularize contact for surface points with small contact forces, as their contact status (penetrated or detached) may easily change from one global iteration to the next [33] and which may cause convergence issues (at the global level). Note also that the transition between the quadratic and cubic part of the potential is smooth, and so is the transition of its derivative.

3.3. Integration of the contact potential over the slave surface.

As contact interactions arise over a finite area, the total contact potential is obtained from the following integral on the slave side:

$$\Pi_{PEN}(\underline{p}^1, \underline{p}^2, \bar{\underline{q}}(\underline{p}^1, \underline{p}^2)) = \int_{\partial S^1} \Pi_{pen}\, dS^1, \tag{14}$$

where ∂S^1 denotes the slave surface and $\bar{\underline{h}}$ denotes the entire projection of the slave surface on the master surface according to Eq. (10).

To numerically evaluate the integral in Eq. (14), numerous slave (quadrature) points are seeded on the surface of the slave body. For each one of them (that is detected as being close enough to the master surface), the projection problem in section 3.1 is solved. If a surface point on the slave surface penetrates the master body, the associated contribution is added to the total contact potential:

$$\Pi_{PEN}(\underline{p}^1, \underline{p}^2, \bar{\underline{q}}(\underline{p}^1, \underline{p}^2)) = \sum_{k=1}^{n} w_k \Pi_{pen/k} \left\| \mathbf{n}_k^1(\underline{h}_k^1) \right\|, \tag{15}$$

where w_k denotes the weight factor and $\mathbf{n}_k^1$ the non-unit normal vector to the surface (which serves as a deformation-dependent weight to the quadrature point). $\Pi_{pen/k}$ denotes the contact potential of the k^{th} slave surface point with local coordinates $\underline{h}_k^1$ and is given by Eq. (13).

3.4. Contact potential's contribution to the weak form

Now that the contact potential between two beams is constructed, its contribution to the weak form needs to be derived. To do so, we consider the variation of Eq. (15) with respect to the kinematic variables of both bodies in contact:

$$\delta\Pi_{PEN}(\underline{p}^1, \underline{p}^2, \bar{\underline{q}}(\underline{p}^1, \underline{p}^2)) = \sum_{k=1}^{n} w_k \delta \left(\Pi_{pen/k} \left\| \mathbf{n}_k^1(\underline{h}_k^1) \right\| \right). \tag{16}$$

The variation of the contact potential for a single quadrature point (from now we omit subscript k) can be expressed as follows:

$$\delta \left(\Pi_{pen} \left\| \mathbf{n}^1(\underline{h}^1) \right\| \right) = \left\| \mathbf{n}^1(\underline{h}^1) \right\| \delta\Pi_{pen} + \Pi_{pen} \delta \left\| \mathbf{n}^1(\underline{h}^1) \right\|. \tag{17}$$

Now we will work out the two parts of this variation. For the ease of the notation, we collect all kinematic variables in $\underline{p}$. Π_{pen} depends explicitly on $\underline{p}$, as well as on $\underline{q}$ (itself depending implicitly on $\underline{p}$ *i.e.* $\underline{q}(\underline{p})$). Its variation can thus be expressed as:

$$\delta\Pi_{pen} = \frac{\partial \Pi_{pen}}{\partial \underline{p}} \cdot \delta\underline{p} + \frac{\partial \Pi_{pen}}{\partial \underline{q}} \cdot \delta\underline{q}. \tag{18}$$

As the primary variables of the problem are the kinematic variables stored in $\underline{p}$ however, the variation must ultimately be expressed in terms of $\delta\underline{p}$. To establish the relationship between $\delta\underline{q}$ and $\delta\underline{p}$, we state that the local residual in Eq. (10) must remain valid for an infinitesimal change of $\underline{p}$. We express this as follows:

$$\delta\mathbf{f}(\bar{\underline{q}}) = \left.\frac{\partial \mathbf{f}}{\partial \underline{p}}\right|_{\bar{\underline{q}}} \delta\underline{p} + \left.\frac{\partial \mathbf{f}}{\partial \underline{q}}\right|_{\bar{\underline{q}}} \delta\bar{\underline{q}} = \mathbf{0}. \tag{19}$$

We can recognize matrix $\underline{\underline{\mathbf{H}}}$ of Eq. (11) in this expression as:

$$\underline{\underline{\mathbf{H}}}(\underline{\bar{q}}) = \left.\frac{\partial \mathbf{f}}{\partial \underline{q}}\right|_{\underline{\bar{q}}}, \tag{20}$$

with the only difference that $\underline{\underline{\mathbf{H}}}$ in Eq. (11) is evaluated at an estimate of $\underline{q}$ (i.e. at $\underline{q}^e$) and here it is evaluated at $\underline{\bar{q}}$. Based on Eq. (19), we can now write:

$$\delta\underline{\bar{q}} = \left(-\underline{\underline{\mathbf{H}}}(\underline{\bar{q}})^{-1} \left.\frac{\partial \mathbf{f}}{\partial \underline{p}}\right|_{\underline{\bar{q}}}\right) \delta\underline{p} = \underline{\underline{A}}\,\delta\underline{p}, \tag{21}$$

such that Eq. (18) can be written as:

$$\begin{aligned} \delta\Pi_{pen} &= \left(\frac{\partial \Pi_{pen}}{\partial \underline{p}}\right) \cdot \delta\underline{p} + \left(\frac{\partial \Pi_{pen}}{\partial \underline{q}}\right) \cdot \underline{\underline{A}}\,\delta\underline{p} \\ &= \delta\underline{p} \cdot \left(\frac{\partial \Pi_{pen}}{\partial \underline{p}} + \underline{\underline{A}} \cdot \frac{\partial \Pi_{pen}}{\partial \underline{q}}\right) \\ &= \delta\underline{p} \cdot \underline{r}. \end{aligned} \tag{22}$$

The issue with this expression is that $\frac{\partial \Pi_{pen}}{\partial \underline{p}}$ is significantly elaborate to derive and hence, its derivation is prone to mistakes. We therefore do not derive $\underline{r}$ analytically but we employ the automatic differentiation technique. With the formalism introduced in [35], we equivalently obtain $\underline{r}$ as follows:

$$\underline{r} = \left.\frac{\hat{\delta}\Pi_{pen}}{\hat{\delta}\underline{p}}\right|_{\frac{\hat{\delta}(\underline{\bar{q}})}{\hat{\delta}\underline{p}} = \underline{\underline{A}}}. \tag{23}$$

Now that we have treated variation $\delta\Pi_{pen}$ in Eq. (17), we continue with variation $\delta \left\|\mathbf{n}^1(\underline{h}^1)\right\|$ in Eq. (17). As $\mathbf{n}^1$ corresponds to the normal vector of a (fixed) slave surface point, it does not depend on $\underline{h}^2$, nor on g_N, so its variation simply reads:

$$\begin{aligned} \delta \left\|\mathbf{n}^1\right\| &= \delta\mathbf{n}^1 \frac{\mathbf{n}^1}{\|\mathbf{n}^1\|} \\ &= \left(\frac{\partial \mathbf{n}^1}{\partial \underline{p}}\right)^T \delta\underline{p}\, \frac{\mathbf{n}^1}{\|\mathbf{n}^1\|} \\ &= \delta\underline{p} \cdot \frac{\partial \mathbf{n}^1}{\partial \underline{p}} \frac{\mathbf{n}^1}{\|\mathbf{n}^1\|} \\ &= \delta\underline{p} \cdot \underline{d}. \end{aligned} \tag{24}$$

In order to compute the consistent tangent matrix of the contact scheme, we again use the automatic differentiation technique (see [35, 36, 37, 38]) which yields:

$$\underline{\underline{K}} = \left.\frac{\hat{\delta}\underline{r}}{\hat{\delta}\underline{p}}\right|_{\frac{\hat{\delta}(\underline{q})}{\hat{\delta}\underline{p}} = \underline{\underline{A}}}. \tag{25}$$

4. Spatial discretization with the Finite Element Method and smoothing of the surface

4.1. Finite Element Discretization

Each beam is now discretized as a string of successive beam finite elements. Each beam element employed in this contribution uses two nodes. Each node comes with a reference location vector, a displacement vector and three rotations. The displacements and rotations form the six kinematic variables of each node. The elements thus use a linear interpolation of (i) $\mathbf{X}_c$, the original location vector of the centroid line, (ii) $\mathbf{u}_c$, the displacement vector of the centroid line, and (iii) $\boldsymbol{\theta}$, the rotation vectors. It is important to mention that, consistent with the beam kinematics in the space continuous setting introduced in section 2, the cross-section does not deform (although its orientation relative to the centroid line can change). It must also be noted that the linear interpolation of the rotation vectors employed here renders the finite-element model slightly strain-variant (see [25] for a discussion). This is in contrast with the strains employed in the space-continuous geometrically exact beam theory (see [22, 23]) that are not affected by rigid translations and rotations.

In the following, we explain how the kinematics introduced in section 2 are interpolated for a single beam element of length $L_{0_{el}}$ in the reference configuration. The reference location of each material point of this beam element is defined by a vector in the local coordinate system attached to the beam centroid line by $\mathbf{h} = \sum_{i=1}^{3} h_i \mathbf{e}_{0i}$ (where $h_1 \in [0, L_{0_{el}}]$), as well as by a vector in the global coordinate system, $\mathbf{X} = \sum_{i=1}^{3} X_i \mathbf{a}_i$.

The interpolation of the reference location of the beam element's centroid line can be expressed as follows:

$$\mathbf{X}_c(h_1) = \underline{N}(h_1) \cdot \underline{\mathbf{X}}, \tag{26}$$

where $\underline{\mathbf{X}}$ denotes the column with the reference location vectors of the beam element's nodes and $\underline{N}$ denotes the column with associated basis functions. The displacement field of the beam element's centroid line can be expressed as follows:

$$\mathbf{u}_c(h_1) = \underline{N}(h_1) \cdot \underline{\mathbf{u}}, \tag{27}$$

where $\underline{\mathbf{u}}$ denotes the column with the displacement vectors of the beam element's nodes. Together, the centroid line in the deformed configuration follows:

$$\mathbf{x}_c(h_1) = \underline{N}(h_1) \cdot (\underline{\mathbf{X}} + \underline{\mathbf{u}}). \tag{28}$$

To locate material points that are not placed on the beam element's centroid line, the orientation of the local basis attached to the sections are needed (see Eq. (4) and (5)). To this end, interpolation of the field of rotation tensors $\boldsymbol{\Lambda}$ is required. As $SO(3)$ is a nonlinear manifold, $\boldsymbol{\Lambda}(h_1)$ cannot be interpolated directly, but is obtained here by applying Rodrigues' formula (see [27]) to the interpolated rotation vector:

$$\boldsymbol{\theta}(h_1) = \underline{N}(h_1) \cdot \underline{\boldsymbol{\theta}} \tag{29}$$

as follows:

$$\boldsymbol{\Lambda}(h_1) = \mathbf{I} + sin\left(\|\boldsymbol{\theta}\|\right) \mathbf{S}(\boldsymbol{\theta}) + \left(1 - cos\left(\|\boldsymbol{\theta}\|\right)\right) \mathbf{S}(\boldsymbol{\theta})\mathbf{S}(\boldsymbol{\theta}), \tag{30}$$

where $\mathbf{I}$ denotes the unit tensor, $\|\bullet\|$ denotes the L_2-norm and $\underline{\boldsymbol{\theta}}$ denotes the column with the nodal rotation vectors. $\boldsymbol{\Lambda}$ denotes the (unique) rotation tensor corresponding to a rotation around the

axis $\frac{\boldsymbol{\theta}}{\|\boldsymbol{\theta}\|}$ by an angle of $\|\boldsymbol{\theta}\|$. $\mathbf{S}$ is skew-symmetric and its matrix form can be furthermore expressed as:

$$\underline{\underline{S}}(\boldsymbol{\theta}(h_1)) = \begin{bmatrix} 0 & -\theta_3(h_1) & \theta_2(h_1) \\ \theta_3(h_1) & 0 & -\theta_1(h_1) \\ -\theta_2(h_1) & \theta_1(h_1) & 0 \end{bmatrix}. \tag{31}$$

Eq. (3) is used to locate points that are not on the beam element's centroid line employing the interpolations of $\mathbf{x}_c$ and $\boldsymbol{\Lambda}$ in Eqs. (28) and (30), respectively.

4.2. Smoothing of the surface

For the type of beam element that we use, local base vector $\mathbf{e}_{01}$ always points in the direction of the beam axis in the initial configuration:

$$\mathbf{e}_{01}(h_1) = \frac{\frac{\partial \underline{\underline{N}}}{\partial h_1} \cdot \underline{\mathbf{x}}_0}{\left\| \frac{\partial \underline{\underline{N}}}{\partial h_1} \cdot \underline{\mathbf{x}}_0 \right\|}. \tag{32}$$

Thus, if a string of successive beam elements is not straight in the reference configuration, its centroid line is C^0-continuous (see Fig. 4). The vector fields of local basis vectors $\mathbf{e}_{01}, \mathbf{e}_{02}, \mathbf{e}_{03}$ are then C^{-1}-continuous. This causes a discontinuity in the orientation of the cross-sections at nodes shared by two elements, meaning that the surface of the string of beams is discontinuous. Contact is then obviously hard to formulate.

To avoid this issue, we introduce a smooth surface, to which contact constraints are applied. This smooth surface also has the advantage that the C^0 or C^{-1}-continuity of the string's surface is replaced by a C^1-continuous surface, which we believe improves the convergence properties of the framework (although we do not compare this in the results section).

In this subsection, the construction of this smooth surface is discussed. It is important to mention that contact is considered for this smooth approximation, instead of the string's actual surface, but that the beam formulation itself remains unchanged. The smoothing approach could thus be applied to other types of beam formulation with some minor changes.

The smoothing procedure uses Bézier curves to smooth the string's centroid line. One Bézier curve is used to smooth the centroid line of two successive beam elements. This entails that if a string consist of n beam elements, $n-1$ Bézier curves are used to smooth the string's centroid line, and by this, the surface. A typical result of this is shown in Fig. 4 for a string of three beams. The smoothing procedure is presented for two adjacent beam elements with indices j and $j+1$. This entails that three nodes are involved. The indices of these nodes are i, $i+1$ and $i+2$.

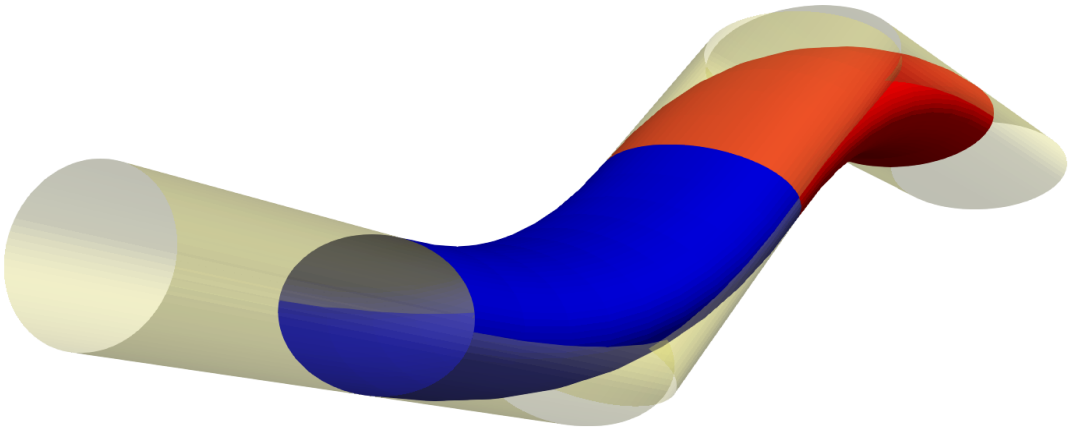

Figure 4: The surface of a string of three beam elements and two smoothed surface.

Reference configuration

The smooth centroid line between two beams in the reference configuration is created using four Bernstein polynomials as follows:

$$\tilde{\mathbf{X}}_c(\eta_1) = \underline{B}(\eta_1) \cdot \underline{\tilde{\mathbf{X}}}_c, \tag{33}$$

where $\underline{B}$ denotes the column that includes the four cubical Bernstein polynomials and $\underline{\tilde{\mathbf{X}}}_c$ denotes the column that contains the original location vectors of the four control points (see fig. 5):

$$\underline{\tilde{\mathbf{X}}}_c = \left[\tilde{\mathbf{X}}_c^0, \tilde{\mathbf{X}}_c^1, \tilde{\mathbf{X}}_c^2, \tilde{\mathbf{X}}_c^3\right]^T \tag{34}$$

with:

$$\tilde{\mathbf{X}}_c^0 = \frac{1}{2}\left(\mathbf{X}_c^i + \mathbf{X}_c^{i+1}\right) \tag{35}$$

$$\tilde{\mathbf{X}}_c^3 = \frac{1}{2}\left(\mathbf{X}_c^{i+1} + \mathbf{X}_c^{i+2}\right) \tag{36}$$

$$\tilde{\mathbf{X}}_c^1 = \tilde{\mathbf{X}}_c^0 + (\mathbf{X}_c^{i+2} - \tilde{\mathbf{X}}_c^0)\alpha \tag{37}$$

$$\tilde{\mathbf{X}}_c^2 = \tilde{\mathbf{X}}_c^2 + (\tilde{\mathbf{X}}_c^3 - \mathbf{X}_c^{i+2})\alpha \tag{38}$$

where $\alpha \in [0, 1]$ denotes a parameter to be selected by the user [39] that dictates the location of the second and third control points in Eqs. (37) and (38). $\eta_1 \in [0, 1]$ parametrises the smoothed centroid line $\tilde{\mathbf{X}}_c \in \mathbb{R}^3$.

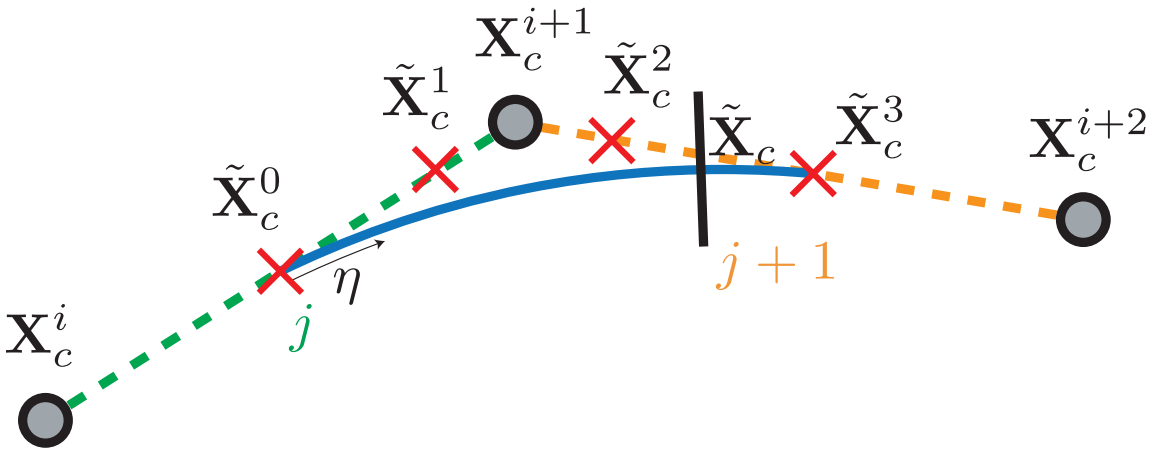

Figure 5: Schematic of a smooth centroid line (plain blue) constructed from the centroid lines of two beam elements (dashed lines) in the reference configuration. The nodes of the elements are indicated by circle and the control points by crosses. A (fictitious) section attached to $\tilde{\mathbf{X}}_c$ is indicated in black.

The neatest would now be to define the first base vector of the local basis normal to the cross-section in the smoothed reference configuration (i.e. $\tilde{\mathbf{e}}_{01}$) as:

$$\tilde{\mathbf{e}}_{01}(\eta_1) = \frac{\frac{\partial \underline{B}}{\partial \eta_1} \cdot \underline{\tilde{\mathbf{X}}}_c}{\left\| \frac{\partial \underline{B}}{\partial \eta_1} \cdot \underline{\tilde{\mathbf{X}}}_c \right\|}, \tag{39}$$

so that cross-sections of the smoothed reference configuration would be orthogonal to the smoothed centroid line. This would however also entail that $\tilde{\mathbf{e}}_{02}$ and $\tilde{\mathbf{e}}_{03}$ need to be set by the user, which can be significantly less straightforward for the smooth Bézier curves than setting $\mathbf{e}_{02}$ and $\mathbf{e}_{03}$ for the beam elements. We therefore determine them for the Bézier approximation of the centroid line as follows:

$$\tilde{\mathbf{e}}_{0i}(\eta_1) = \underline{B}(\eta_1) \cdot \underline{\tilde{\mathbf{e}}}_{0i}, \tag{40}$$

where $\underline{\tilde{\mathbf{e}}}_{0i}$, $i \subset \{1, 2, 3\}$ denotes the column that stores $\mathbf{e}_{0i}$ at the four control points. For linearly interpolated beam elements $\underline{\tilde{\mathbf{e}}}_{0i}$ contains four times the same base vector for an initially straight strings of beams, and two different base vectors otherwise.

The location vectors of the material points of the string in the smoothed reference configuration are then given by:

$$\tilde{\mathbf{X}}(\underline{\eta}) = \tilde{\mathbf{X}}_c(\eta_1) + \tilde{\mathbf{V}}(\underline{\eta}), \tag{41}$$

where

$$\tilde{\mathbf{V}}(\underline{\eta}) = \eta_2 \tilde{\mathbf{e}}_{02}(\eta_1) + \eta_3 \tilde{\mathbf{e}}_{03}(\eta_1), \tag{42}$$

where $\tilde{\mathbf{V}}$ denotes a vector connecting $\tilde{\mathbf{X}}_c$ to a point on the perimeter of the (fictitious) section attached to this centroid point (see fig. 6), and $\underline{\eta} = \{\eta_1, \eta_2\} \in [0,1] \times [0, 2\pi]$ denotes a column of two local variables parametrising the smooth patch's surface (see Fig. 6).

Deformed configuration

To determine the smoothed centroid line in the deformed configuration, we also need the smoothed displacement field of the centroid line, which is expressed as:

$$\tilde{\mathbf{u}}_c(\eta_1) = \underline{B}(\eta_1) \cdot \underline{\tilde{\mathbf{u}}}_c, \tag{43}$$

where $\underline{\tilde{\mathbf{u}}}_c$ denotes the column of displacement vectors at the four control points. The smoothed centroid line in the deformed configuration can then be written as:

$$\tilde{\mathbf{x}}_c(\eta_1) = \tilde{\mathbf{X}}_c(\eta_1) + \tilde{\mathbf{u}}_c(\eta_1) = \underline{B}(\eta_1) \cdot (\underline{\tilde{\mathbf{X}}}_c + \underline{\tilde{\mathbf{u}}}_c). \tag{44}$$

To locate all material points in the approximated deformed configuration, instead of just those on the centroid line, we also need to smooth the rotation vector field, for which we similarly write:

$$\tilde{\boldsymbol{\theta}}_c(\eta_1) = \underline{B}(\eta_1) \cdot \underline{\tilde{\boldsymbol{\theta}}}, \tag{45}$$

where $\underline{\tilde{\boldsymbol{\theta}}}$ denotes the rotation vectors at the four control points. Corresponding rotation tensor $\tilde{\boldsymbol{\Lambda}}(\eta_1)$ can then again be determined using Rodrigues' formula (Eq. (30)).

The location vectors of the material points of the string in the smoothed deformed configuration can now be written as (see Fig. 6):

$$\tilde{\mathbf{x}}(\mathbf{h}) = \tilde{\mathbf{x}}_c(\eta_1) + \tilde{\mathbf{v}}(\boldsymbol{\eta}), \tag{46}$$

where

$$\tilde{\mathbf{v}}(\underline{\eta}) = \tilde{\boldsymbol{\Lambda}}(\eta_1)(\eta_2 \tilde{\mathbf{e}}_{02}(\eta_1) + \eta_3 \tilde{\mathbf{e}}_{03}(\eta_1)). \tag{47}$$

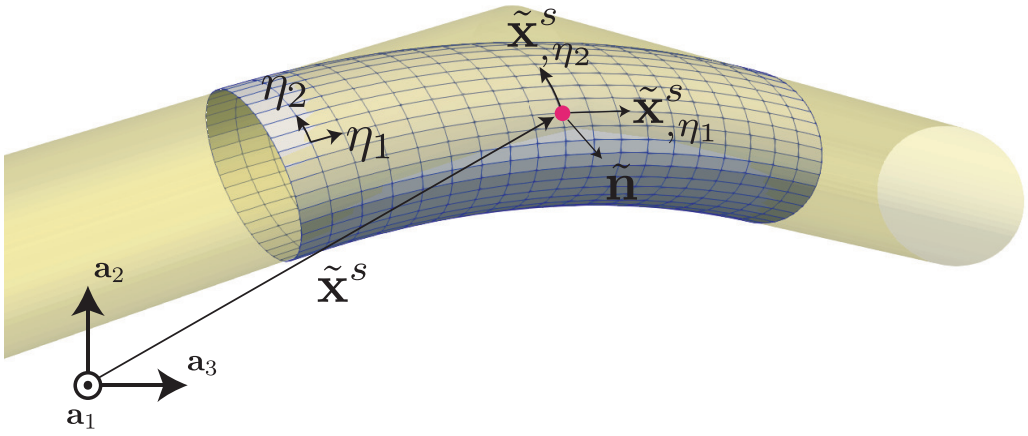

Figure 6: A surface point $\tilde{\mathbf{x}}^s$ and its local surface basis $\{\tilde{\mathbf{x}}^s_{,\eta_1}, \tilde{\mathbf{x}}^s_{,\eta_2}, \tilde{\mathbf{n}}^s\}$. The surface of the two beams from which the smooth surface is constructed are presented in yellow.

Note that vector $\tilde{\mathbf{v}}$ is generally not in the plane normal to $\tilde{\mathbf{x}}_c$, because, as stated above, the (pseudo) cross-sections are in general not normal to the smoothed centroid line in the reference configuration, but also because of the relative rotation of the (pseudo) cross-section around the (pseudo) centroid point $\tilde{\mathbf{x}}_c$.

To adapt the contact framework to the smoothed geometry introduced above, one needs to replace the local coordinates in $\underline{h}$ by the local coordinates of the smooth surface $\underline{\eta}$. For an integration point, $\tilde{\mathbf{x}}^{s1}$, on the slave side with local coordinates $\underline{\eta}^1$, the procedure is as follows:

- The projection point of $\tilde{\mathbf{x}}^{s1}$ on the master surface, $\tilde{\mathbf{x}}^{s2}(\bar{\underline{h}}^2)$, is found by solving the local problem in Eq. (10) adapted to the smoothed surfaces, i.e. the column of local parameters $\bar{\underline{q}}$ to solve for is now $\bar{\underline{q}} = [\bar{\eta}_1^2, \bar{\eta}_2^2, \bar{g_N}]$,
- If $\tilde{\mathbf{x}}^{s1}$ is penetrated, the contribution of this integration point to weak form is computed using Eq. (17). The kinematic variables involved are the nodal degrees of freedom used to construct the smooth patches that are stored in columns $\underline{p}^1$ and $\underline{p}^2$. Three beam nodes are necessary to construct each patch so that $\underline{p}^1$ and $\underline{p}^2$ have 18 components each. Consequently, contact residual $\underline{r}$ in Eq. (23) has a length of 36 and the dimensions of contact tangent matrix $\underline{\underline{K}}$ are 36×36.

5. Numerical Results

In the current section, we present initial results that can be achieved with the contact scheme. We first focus on two strings of successive beam elements that come in contact with each other under different loading conditions. Second, we focus on the twisting of several parallel strings of successive beam elements as a simplified manufacturing process for wire ropes.

Different possibilities exist to place quadrature points. At the beginning of each time step, integration points could be placed in the region where beams' surfaces are close to each other. This would entail several update of the integration points' surface coordinates.

Another option, that is less accurate but computationally less expensive is to compute the coordinates and weights of a grid of integration points on the entire beam surface in the undeformed configuration. This means that the number of quadrature points is constant and that their surface coordinates and weight do not need to be recomputed. This approach that has been adopted in the following numerical examples.

5.1. Two orthogonal strings

In the first example, we consider two beams with elliptical cross-sections denoted by A and B (see Fig. 7) discretised with strings of successive beam elements. These strings are initially orthogonal in space, and they both have the same geometrical properties (length and dimensions of the sections), mechanical properties and discretisation (see ahead to the top row of Fig. 10). The aim of this numerical example is to show that the presented scheme is able to treat contact problems in which large sliding displacements occur (i.e. slave points in contact can slide from one smooth surface approximation to another), whilst the deformation of the contacting surfaces is substantial. The geometrical and material parameters are, together with the numerical parameters of the discretisation and the contact scheme, presented in Tables 1 and 2. Various Dirichlet boundary conditions (BCs) are applied at the end nodes of string A during the interval of (fictitious) time $t \in [0, 6]$. The kinematic variables of the end nodes of string B are retained. We apply the following Dirichlet BCs to string A (see Fig. 8):

- $t = 0$: the strings are slightly detached; $\bar{g}_N \approx 0$ in the middle of the strings at a single surface point.
- $0 < t \leq 1$: the end nodes are moved by 1.5 cm in $\mathbf{a}_2$-direction.
- $1 < t \leq 2$: the end nodes are moved in $[1, 0, 1]$ direction by 1 cm.
- $2 < t \leq 3$: the centroid point in the middle of string A is used as the center of rotation of string A around $\mathbf{a}_2$ with an amplitude of $\frac{\pi}{3}$. This rotation is applied to nodes at the end string A.
- $3 < t \leq 4$: the end nodes undergo the reverse rotation around the same axis of rotation.
- $4 < t \leq 5$: the end nodes undergo the reverse displacement as the one that was performed for $1 < t \leq 2$.
- $5 < t \leq 6$: the end nodes are moved vertically until the two strings completely detach.

The number of quadrature points placed on the surface of each slave patch (at fixed material coordinates) to evaluate Eq. (15) is given in Table 2. The number of surface points is important because at the beginning of the interval $0 < t \leq 1$ and at the end of the interval $5 < t \leq 6$, contact may be localised and hence, contact may be poorly approximated with a coarse grid of surface points.

Table 2 also provides the initial penalty stiffness employed. This value should be related to the mechanical parameters of the contacting bodies as well as the geometrical features of the surfaces at the contact area and the penetration [40] (note that a penalty stiffness directly dependent

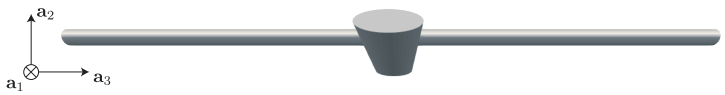

Figure 7: Initial configuration.

on the kinematic variables would result in more complex expressions for $\underline{r}$ and $\underline{\underline{K}}$). Here, the penalty stiffness is adapted if the local penetration measured for one or several of the slave points is larger than a certain user-defined threshold. In the present case, we choose to increase the penalty stiffness by 10% if the penetration is larger than 5% of the smallest cross-sectional radius (see also [33] for another example of regularization of the contact constraint by increasing the penalty stiffness). The update of the penalty stiffness is performed after an increment of the global solver has converged. Directly after the update, the nodal equilibrium is again solved for, since the increase of the penalty stiffness results in a loss of equilibrium. Additional iterations are therefore needed to restore force equilibrium before moving to the next increment. If, after convergence with this new penalty stiffness, the violation of contact constraint $\bar{g}_N$ is still too large, the process is repeated.

The configurations after each second of the fictitious time are presented in Fig. 10. Contact tractions in the contact area are presented in Fig. 9 for $t = 1, 2$ and 3 seconds. The evolution of two components of the reaction forces at the end nodes of a string are presented in the top diagrams of Fig. 11. The number of active contact points is presented in the same figure. During the 1^{st} second, contact does not change location but increases in magnitude over time. This can be observed by the substantial increase of the number of active slave points during the first half of the 1^{st} second (bottom-left diagram in Fig. 3). Consequently, the reaction force in $\mathbf{a}_2$-direction (top-right diagram in Fig. 3) increases qualitatively almost the same as the number of penetrating surface points. During the second half of the first second, the number of penetrating points oscillates. This is due to the adjustment of the penalty stiffness.

During the 2^{nd} second ($1 < t \leq 2$), string A slides with respect to string B. Consequently, the number of penetrating surface points remains similar, which is to expected. The reaction force in $\mathbf{a}_2$ direction reduces somewhat, whilst the reaction force in $\mathbf{a}_1$ direction slightly increases. Concluding we can state that the contact framework is able to accurately treat large sliding displacements (penetrating slave points can move from one surface approximation to another and new slave points become active, whilst active ones become inactive).

In the 3^{rd} second ($2 < t \leq 3$), the location of the contact area remains largely at the same location, but the contact area increases due to the prescribed rotation. We nevertheless see a decrease of the number of active slave points, because the employed grid of slave points has a wider spacing in the string's longitudinal direction than in the tangential direction. The change of contact area has substantial influences on the reaction forces. The interesting issue here is that the present loading would have no influence on the reaction forces for a point-wise contact scheme (which would not work to begin with because contact does not occur at a single point), except for the trigonometric change of the reaction forces.

In the last 3 seconds, the entire loading is reversed and consequently, we see that the reaction-force time diagrams are symmetrical around $t = 3$. Once again, the reason that the number of active slave points is not symmetrical is because the penalty stiffness is increased if necessary, but not reduced if possible. These results are highly satisfactory.

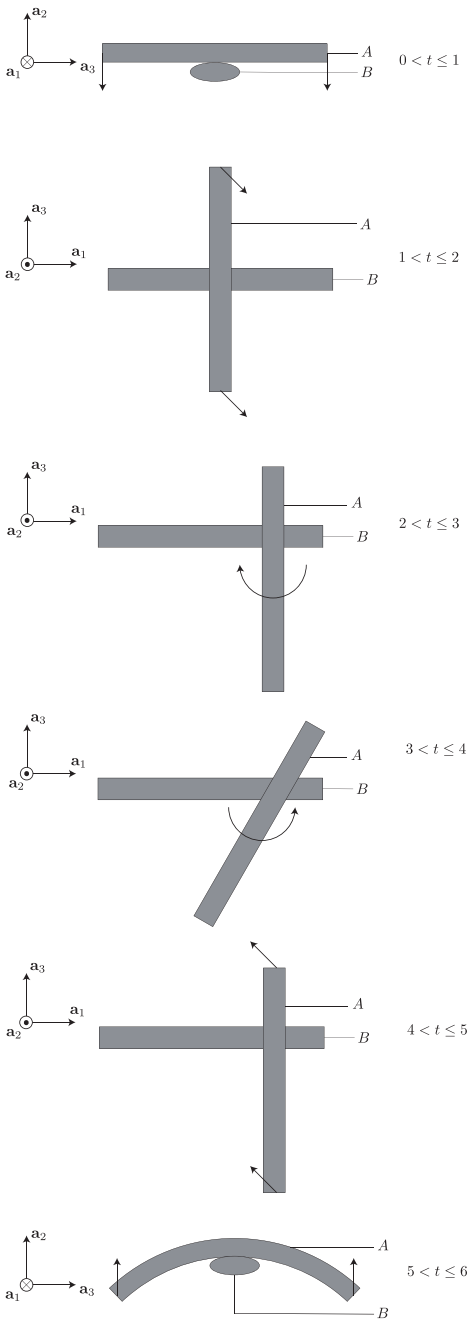

Figure 8: Boundary conditions applied during the different phases of the loading. The schematics are not to scale.

Beam length (cm)	8
Radius 1 of the elliptical cross-section(cm)	0.6
Radius 2 of the elliptical cross-section (cm)	0.2
Young's modulus (GPa)	100
Poisson's ratio	0.3
Beams Finite Elements per beam	60

Table 1: General properties of each beam.

Surface points in axial direction	5
Surface points in tangential direction	80
α	$\frac{2}{3}$
Initial ϵ (GPa)	10

Table 2: Contact parameters.

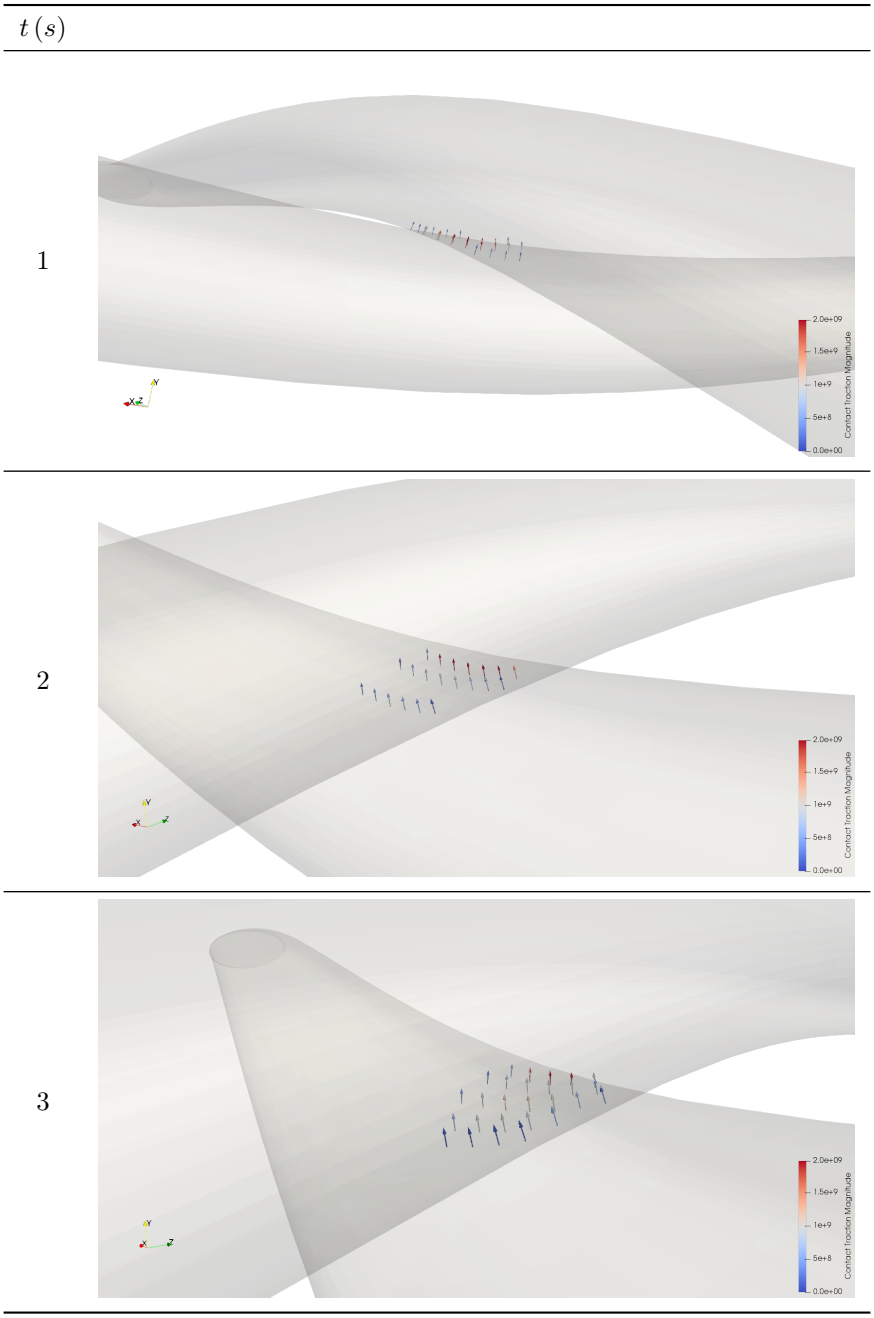

Figure 9: Contact tractions acting in the direction of the normal to the slave surface at the quadrature points for different times of the simulation.

$t(s)$	Top view	Side view	Perspective
0	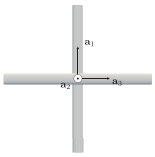	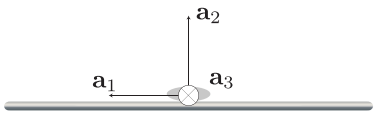	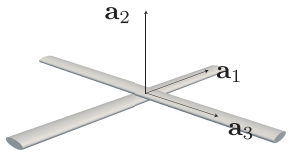
1	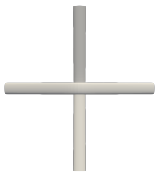		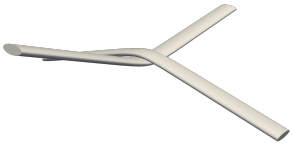
2	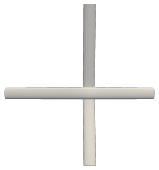		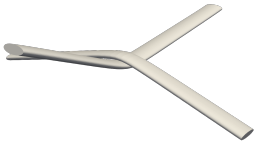
3	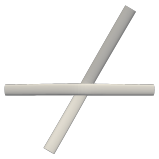		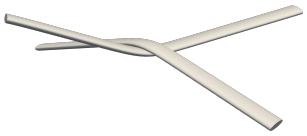
4	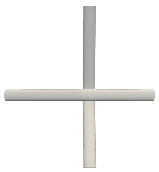		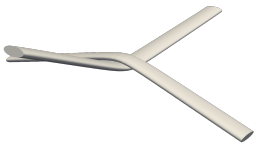
5	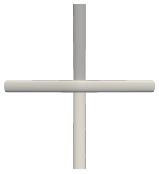		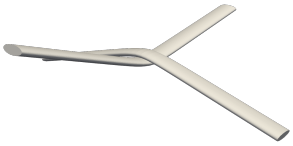

Figure 10: Three views of the deformed beams after different pseudo-times (without scaling of the deformations).

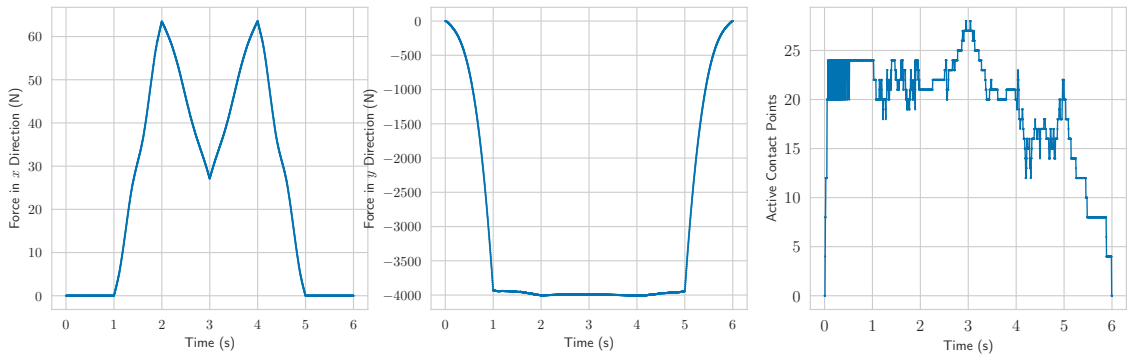

Figure 11: Evolution of the reaction force in $\mathbf{a}_2$ direction (left) and in $\mathbf{a}_1$ direction (middle). Evolution of the number of active contact points (right). Note that the order of magnitude of the forces in the left and central diagram is a factor of two different.

5.2. Twisting

In the next example, we consider two setups of several parallel beams which are twisted (see Fig. 13). For setup A, the central beam has a circular cross-section and the beams around it have an elliptical cross-section. In setup B however, the central beam is elliptical and the peripheral beams have a circular section. For both setups, the central beams have the same section area. Similarly, each peripheral beam in setup A has the same cross-sectional area as the peripheral beams in setup B.

The cross-sections at the two ends of the beams are rigidly rotated around the longitudinal beams' direction in the reference configuration with an amplitude of π. The planes containing these sections are kept at a constant distance during the simulation. This problem is challenging for a contact framework as the contact forces increase substantially, the contact is non-local and contacting surfaces increasingly deform and curve during time.

The employed beam properties are presented in Table 3. The initial and final configurations are shown in Fig. 13. Fig. 14 shows the evolution of the total reaction force in longitudinal direction and the total torque at one of the end sections. The evolution of the number of penetrated contact points is also presented. The results clearly show that the cross-sectional shape has a major influence on the simulation results.

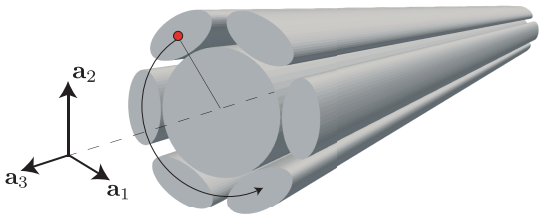

Figure 12: Illustration of the Dirichlet boundary condition applied to one end of one discretized beam (red circle). The rotation of Π around the axis of rotation (dashed line) applied incrementally is illustrated with the black arrow.

	Central Beam	Peripheral Beams
Beam length (cm)	15	15
Radius 1 of the elliptical cross-section (cm)	0.5	$\frac{3}{10}$
Radius 2 of the elliptical cross-section (cm)	0.5	$\frac{3}{20}$
Young's modulus (GPa)	100	100
Poisson's ratio	0.3	0.3
Beam finite elements per beam	60	60

(a) Setup A.

	Central Beam	Peripheral Beams
Beam length (cm)	15	15
Radius 1 of the elliptical cross-section (cm)	$\frac{2}{3}$	$\frac{1}{3\sqrt{200}}$
Radius 2 of the elliptical cross-section (cm)	$\frac{3}{8}$	$\frac{1}{3\sqrt{200}}$
Young's modulus (MPa)	1000	1000
Poisson's ratio	0.3	0.3
Beam finite elements per beam	60	60

(b) Setup B.

Surface points in axial direction	4
Surface points in tangential direction	80
α	$\frac{2}{3}$
Initial ϵ (MPa)	100

(c) Contact properties of each slave patch.

Table 3: Properties of the beams used for the twisting.

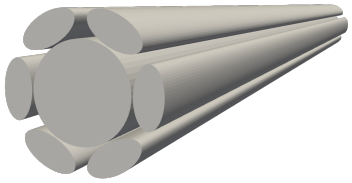

(a) setup A, $t = 0$.

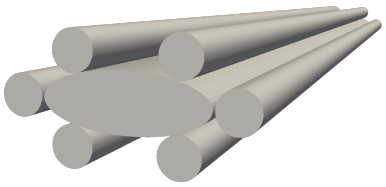

(b) setup B, $t = 0$.

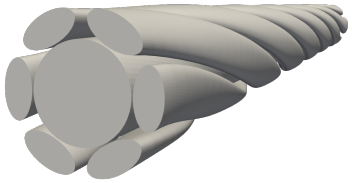

(c) setup A, $t = t_{final}$.

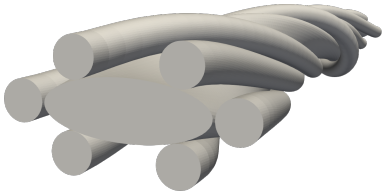

(d) setup B, $t = t_{final}$.

(e) setup A, $t = t_{final}$, side view.

(f) setup B, $t = t_{final}$, side view.

Figure 13: Setup A and B in their initial and final configuration.

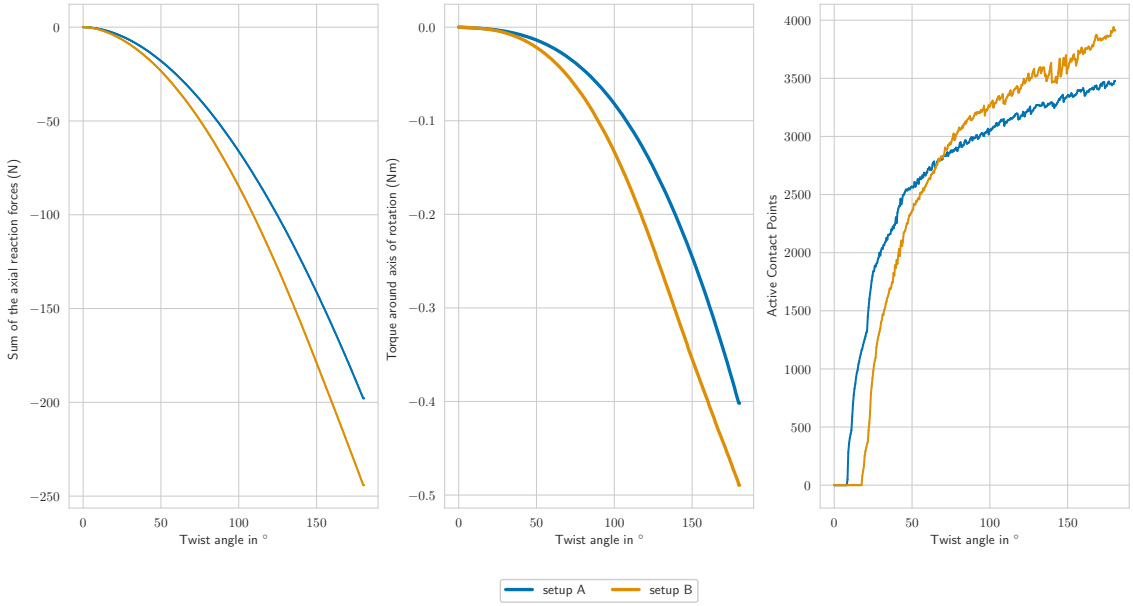

Figure 14: Left: Axial reaction forces; Middle: The reaction torque around the axis of rotation; Right: evolution of the number of active contact points.

6. Conclusion

Slender structural components are typically represented by beams in mechanical models, in turn discretized with beam finite elements. They are often characterized by circular cross-sections, but elliptical cross-sections are regularly required instead. Contact between shear-deformable beams with elliptical cross-sections cannot only be based on the centroid lines, as is most often done in contact schemes for beams with circular cross-sections.

The contact framework proposed in this work therefore relies on the surface of the beams. It allows to deal with scenarios in which the distance between the contacting surfaces has no clear minimum, as is the case for parallel beams for example. Thus, this contribution is a first attempt to complete the frameworks of [19, 20], which are limited by the assumption of a unique contact location.

Our framework places points on one of the two surfaces candidates for contact (slave) and then projects them on the other surface (the master). This projection differs from the conventional closest point projection (CPP), because the CPP is not unique and may change drastically for small variations (in case of non-circular cross-sections). Instead, we determine the amount of penetration based on surface points and a point on the centroid line.

Since the employed geometrically exact beam elements furthermore use a linear interpolation of the kinematic variables, the associated surface of a string may be C^0-continuous in the deformed configuration and even C^{-1}-continuous in the reference and deformed configuration. To overcome this issue, a smoothing procedure of the strings' surfaces is formulated that makes the surfaces C^1-continuous.

The proposed contact approach is computationally more demanding than the approaches of [19, 20] due to the seeding of many points for which penetration is considered. If no unique maximum penetration occurs, as is the case for many practical applications on the other hand, a less efficient approach than [19, 20] appears to be unavoidable. Future work will therefore focus on more efficient generations of surface points and the optimisation of the implementation.

Acknowledgment

The authors gratefully acknowledge the financial support of the University of Luxembourg for project TEXTOOL.

References

[1] L. A. A. Beex and R. Peerlings, "On the influence of delamination on laminated paperboard creasing and folding," *Philosophical Transactions of the Royal Society A: Mathematical, Physical and Engineering Sciences*, vol. 370, no. 1965, pp. 1912–1924, 2012.

[2] P. Mäkelä and S. Östlund, "Orthotropic elastic-plastic material model for paper materials," *International Journal of Solids and Structures*, vol. 40, pp. 5599–5620, oct 2003.

[3] B. Thakkar, L. Gooren, R. Peerlings, and M. Geers, "Experimental and numerical investigation of creasing in corrugated paperboard," *Philosophical Magazine*, vol. 88, pp. 3299–3310, oct 2008.

[4] K.-Y. Lee, Y. Aitomäki, L. A. Berglund, K. Oksman, and A. Bismarck, "On the use of nanocellulose as reinforcement in polymer matrix composites," *Composites Science and Technology*, vol. 105, pp. 15–27, dec 2014.

[5] A. Kulachenko and T. Uesaka, "Direct simulations of fiber network deformation and failure," *Mechanics of Materials*, vol. 51, pp. 1–14, aug 2012.

[6] L. A. A. Beex, R. Peerlings, K. van Os, and M. Geers, "The mechanical reliability of an electronic textile investigated using the virtual-power-based quasicontinuum method," *Mechanics of Materials*, vol. 80, pp. 52–66, jan 2015.

[7] B. Ben Boubaker, B. Haussy, and J. Ganghoffer, "Discrete models of woven structures. Macroscopic approach," *Composites Part B: Engineering*, vol. 38, pp. 498–505, jun 2007.

[8] P. Boisse, A. Gasser, and G. Hivet, "Analyses of fabric tensile behaviour: determination of the biaxial tension-strain surfaces and their use in forming simulations," *Composites Part A: Applied Science and Manufacturing*, vol. 32, pp. 1395–1414, oct 2001.

[9] X. Q. Peng and J. Cao, "A continuum mechanics-based non-orthogonal constitutive model for woven composite fabrics," *Composites Part A: Applied Science and Manufacturing*, vol. 36, pp. 859–874, jun 2005.

[10] Y. Miao, E. Zhou, Y. Wang, and B. A. Cheeseman, "Mechanics of textile composites: Microgeometry," *Composites Science and Technology*, vol. 68, pp. 1671–1678, jun 2008.

[11] A. Jung, E. Lach, and S. Diebels, "New hybrid foam materials for impact protection," *International Journal of Impact Engineering*, vol. 64, pp. 30–38, feb 2014.

[12] A. Jung, L. A. A. Beex, S. Diebels, and S. P. A. Bordas, "Open-cell aluminium foams with graded coatings as passively controllable energy absorbers," *Materials & Design*, vol. 87, pp. 36–41, dec 2015.

[13] Y. Sun, R. Burgueño, W. Wang, and I. Lee, "Modeling and simulation of the quasi-static compressive behavior of Al/Cu hybrid open-cell foams," *International Journal of Solids and Structures*, vol. 54, pp. 135–146, feb 2015.

[14] P. R. Onck, R. Van Merkerk, J. T. M. De Hosson, and I. Schmidt, "Fracture of metal foams: In-situ testing and numerical modeling," in *Advanced Engineering Materials*, vol. 6, pp. 429–431, John Wiley & Sons, Ltd, jun 2004.

[15] M. F. Ashby, "The properties of foams and lattices," *Philosophical Transactions of the Royal Society A: Mathematical, Physical and Engineering Sciences*, vol. 364, pp. 15–30, jan 2006.

[16] L. A. A. Beex, P. Kerfriden, T. Rabczuk, and S. P. A. Bordas, "Quasicontinuum-based multiscale approaches for plate-like beam lattices experiencing in-plane and out-of-plane deformation," *Computer Methods in Applied Mechanics and Engineering*, vol. 279, pp. 348–378, sep 2014.

[17] L. A. A. Beex, O. Rokoš, J. Zeman, and S. P. A. Bordas, "Higher-order quasicontinuum methods for elastic and dissipative lattice models: uniaxial deformation and pure bending," *GAMM-Mitteilungen*, vol. 38, pp. 344–368, sep 2015.

[18] V. Mozafary, P. Payvandy, and M. Rezaeian, "A novel approach for simulation of curling behavior of knitted fabric based on mass spring model," *The Journal of The Textile Institute*, vol. 109, pp. 1620–1641, dec 2018.

[19] A. Gay Neto, P. M. Pimenta, and P. Wriggers, "A master-surface to master-surface formulation for beam to beam contact. Part I: frictionless interaction," *Computer Methods in Applied Mechanics and Engineering*, vol. 303, pp. 400–429, may 2016.

[20] A. Gay Neto, P. M. Pimenta, and P. Wriggers, "A master-surface to master-surface formulation for beam to beam contact. Part II: Frictional interaction," *Computer Methods in Applied Mechanics and Engineering*, vol. 319, pp. 146–174, 2017.

[21] G. Zavarise and L. De Lorenzis, "The node-to-segment algorithm for 2D frictionless contact: Classical formulation and special cases," *Computer Methods in Applied Mechanics and Engineering*, vol. 198, pp. 3428–3451, sep 2009.

[22] J. Simo, "A finite strain beam formulation. The three-dimensional dynamic problem. Part I," *Computer Methods in Applied Mechanics and Engineering*, vol. 49, pp. 55–70, may 1985.

[23] J. Simo and L. Vu-Quoc, "A three-dimensional finite-strain rod model. part II: Computational aspects," *Computer Methods in Applied Mechanics and Engineering*, vol. 58, pp. 79–116, oct 1986.

[24] J. Simo and L. Vu-Quoc, "A Geometrically-exact rod model incorporating shear and torsion-warping deformation," *International Journal of Solids and Structures*, vol. 27, no. 3, pp. 371–393, 1991.

[25] G. Jelenić and M. Crisfield, "Geometrically exact 3D beam theory: implementation of a strain-invariant finite element for statics and dynamics," *Computer Methods in Applied Mechanics and Engineering*, vol. 171, pp. 141–171, mar 1999.

[26] A. Ibrahimbegović, "On finite element implementation of geometrically nonlinear Reissner's beam theory: three-dimensional curved beam elements," *Computer Methods in Applied Mechanics and Engineering*, vol. 122, pp. 11–26, apr 1995.

[27] I. Romero, "The interpolation of rotations and its application to finite element models of geometrically exact rods," *Computational Mechanics*, vol. 34, pp. 121–133, jul 2004.

[28] C. Meier, A. Popp, and W. A. Wall, "Geometrically Exact Finite Element Formulations for Slender Beams: Kirchhoff-Love Theory Versus Simo-Reissner Theory," *Archives of Computational Methods in Engineering*, vol. 26, pp. 163–243, jan 2019.

[29] P. Wriggers, *Computational Contact Mechanics*. Berlin, Heidelberg: Springer Berlin Heidelberg, 2006.

[30] G. Zavarise and P. Wriggers, "A segment-to-segment contact strategy," *Mathematical and Computer Modelling*, vol. 28, pp. 497–515, aug 1998.

[31] G. Zavarise and P. Wriggers, "Contact with friction between beams in 3-D space," *International Journal for Numerical Methods in Engineering*, vol. 49, pp. 977–1006, nov 2000.

[32] A. Konyukhov, O. Mrenes, and K. Schweizerhof, "Consistent development of a beam-to-beam contact algorithm via the curve-to-solid beam contact: Analysis for the nonfrictional case," *International Journal for Numerical Methods in Engineering*, vol. 113, pp. 1108–1144, feb 2018.

[33] D. Durville, "Contact Modelling in Entangled Fibrous Materials," in *Trends in Computational Contact Mechanics*, pp. 1–22, Springer, Berlin, Heidelberg, 2011.

[34] T. Vu, D. Durville, and P. Davies, "Finite element simulation of the mechanical behavior of synthetic braided ropes and validation on a tensile test," *International Journal of Solids and Structures*, vol. 58, pp. 106–116, apr 2015.

[35] J. Lengiewicz, J. Korelc, and S. Stupkiewicz, "Automation of finite element formulations for large deformation contact problems," *International Journal for Numerical Methods in Engineering*, vol. 85, aug 2010.

[36] J. Lengiewicz and S. Stupkiewicz, "Efficient model of evolution of wear in quasi-steady-state sliding contacts," *Wear*, vol. 303, pp. 611–621, jun 2013.

[37] J. Korelc, "Automation of primal and sensitivity analysis of transient coupled problems," *Computational Mechanics*, vol. 44, pp. 631–649, oct 2009.

[38] J. Korelc, "Multi-language and multi-environment generation of nonlinear finite element codes," *Engineering with Computers*, vol. 18, no. 4, pp. 312–327, 2002.

[39] P. Wriggers, L. Krstulovic-Opara, and J. Korelc, "Smooth C1-interpolations for two-dimensional frictional contact problems," *International Journal for Numerical Methods in Engineering*, vol. 51, pp. 1469–1495, aug 2001.

[40] V. L. Popov, *Contact Mechanics and Friction*, vol. 52. Berlin, Heidelberg: Springer Berlin Heidelberg, 2010.

[41] S. Varrette, P. Bouvry, H. Cartiaux, and F. Georgatos, "Management of an academic HPC cluster: The UL experience," in *2014 International Conference on High Performance Computing & Simulation (HPCS)*, pp. 959–967, IEEE, jul 2014.